Pinning and gyration dynamics of magnetic vortices revealed by correlative Lorentz and bright-field imaging

Marcel Möller,* John H. Gaida, and Claus Ropers†
Max Planck Institute for Biophysical Chemistry, 37077 Göttingen, Germany
4th Physical Institute-Solids and Nanostructures,
University of Göttingen, 37077 Göttingen, Germany
(Dated: January 13, 2022)

Topological magnetic textures are of great interest in various scientific and technological fields. To allow for precise control of nanoscale magnetism, it is of great importance to understand the role of intrinsic defects in the host material. Here, we use conventional and time-resolved Lorentz microscopy to study the effect of grain size in polycrystalline permalloy films on the pinning and gyration orbits of vortex cores inside magnetic nanoislands. To assess static pinning, we use in-plane magnetic fields to shift the core across the island while recording its position. This enables us to produce highly accurate two-dimensional maps of pinning sites. Based on this technique, we can generate a quantitative map of the pinning potential for the core, which we identify as being governed by grain boundaries. Furthermore, we investigate the effects of pinning on the dynamic behavior of the vortex core using stroboscopic Lorentz microscopy, harnessing a new photoemission source that accelerates image acquisition by about two orders of magnitude. We find characteristic changes to the vortex gyration in the form of increased dissipation and enhanced bistability in samples with larger grains.

Keywords: Magnetic vortices; Grain boundaries; Pinning; Magnetization dynamics; Transmission electron microscopy; Lorentz microscopy

I. INTRODUCTION

Microscopic magnetic objects such as vortices [1–3] and skyrmions [4–6] have attracted a sustained interest in the past decade. Due to their stability and unique topological properties, these textures have sparked ideas for a vast number of technological applications such as (racetrack) memories [7–10], logical-gates [11, 12] and neuromorphic computing [13]. While various control schemes for the manipulation of these textures by means of external magnetic fields [14, 15], electrical currents [16–18], or optical pulses [3, 18, 19] are widely established, studies probing their interaction with defects are still highly sought after.

Previous investigations addressed the influence of artificial [20–23] and intrinsic [24–30] defects on the static pinning [20, 21, 23, 24] and the dynamics of magnetic vortices [22, 25–28, 31]. A majority of these studies utilized magneto-optical microscopy [25–29], which helped, for example, to link pinning to surface roughness in soft magnetic samples [27]. Higher real-space resolution is offered by spin-polarized scanning tunneling microscopy in scenarios with atomic-scale defects on flat surfaces [23, 32]. This method revealed a Sombrero-shaped pinning potential between vortex cores and surface adsorbates [23]. Excellent spatial resolution for polycrystalline samples with higher surface roughness is possible using electron microscopy techniques [33] and was used to characterize core pinning via one-dimensional differential-phase-contrast line scans [21]. Moreover, recent advances in time-resolved Lorentz microscopy enable imaging magnetic dynamics at simultaneous high spatial and temporal resolution [34–39]. To date, however, the full capabilities of electron microscopy in both magnetic and structural imaging have yet to be leveraged in correlated studies.

In this work, we investigate the influence of the microcrystalline structure of permalloy thin films on the pinning of vortex cores by correlating the grain structure in bright-field images to the magnetic configuration in Lorentz micrographs. In order to obtain maps of pinning sites, we developed TRaPS (**T**EM **Ra**stering of **P**inning **S**ites). This procedure locates defects by laterally shifting the vortex core across a nanostructure and imaging its position with high resolution. This allows us to directly calculate a quantitative two-dimensional representation of the pinning potential. Moreover, we use time-resolved Lorentz microscopy with an improved photoemission source to assess the effect of grain size on the core gyration. We find that annealing leads to a more corrugated pinning potential and larger average distances between pinning sites. Our findings suggest preferential pinning at grain boundaries and vortex orbits that avoid particularly large grains, demonstrating the combined strengths of correlated and *in-situ* magnetic and structural characterization.

* marcel.moeller@uni-goettingen.de
† claus.ropers@mpibpc.mpg.de

II. METHODS

A. Sample System

The sample system we investigate is a magnetic vortex confined in a square permalloy ($Ni_{80}Fe_{20}$) nanoisland [1, 2]. A magnetic vortex is a flux-closure type domain configuration which is predominantly oriented in-plane and curls either counter-clockwise ($c = +1$) or clockwise ($c = -1$) around its central core. At the core region, the magnetization rotates out-of-plane and, either points up or down, said to have a polarization of $p = +1$ or $p = -1$, respectively [2].

A schematic representation of the sample is depicted in Figs. 1 a,b (light and scanning-electron images of the sample are in Supp. Fig. 4). The permalloy square has a thickness of 30 nm and an edge length of 2 µm. To electronically excite the sample, we overlap 100 nm thick gold contacts on two opposing sides of the square, which extend to wire-bonding pads. The nanoisland is positioned at the center of a 15 µm × 15 µm large amorphous silicon nitride window. At a thickness of 30 nm the window is near electron-transparent and is supported by a 200 µm thick silicon frame.

The sample fabrication processes involve electron-beam lithography using a positive-tone electron resist as well as electron-beam and thermal evaporation for the deposition of permalloy and gold, respectively. We take special care to remove any resist prior to metal deposition by subjecting the developed sample to a short oxygen plasma.

The contacts on either side of the microstructure allow us to excite the vortex with in-plane RF-currents, forcing its core on an elliptical trajectory [40–42]. This gyrotropic motion is a consequence of a combination of spin-transfer torques and current-induced Oersted fields [41, 43]. Generally, these systems allow for a resonance frequency between 10 MHz and 10 GHz, depending on the material and nanostructure size. For the parameters of the current sample, we expect resonance frequencies around 100 MHz [37].

To identify the effects of the nanocrystalline structure on the pinning of vortex core, we investigate one annealed sample **A** as well as two non-annealed samples **N1** and **N2**. We prepared all three samples under identical conditions on the same silicon frame. Annealing is carried out by heating a single nanostructure using a low-frequency alternating current and monitoring the progress via a resistance measurement (for further details, see Suppl. Note 2).

B. TRaPS

We introduce "**T**EM **Ra**stering of **P**inning **S**ites" (TRaPS) as a method to identify and locate static magnetic pinning sites using Fresnel-mode Lorentz microscopy [44, 45]. For our sample, this imaging method

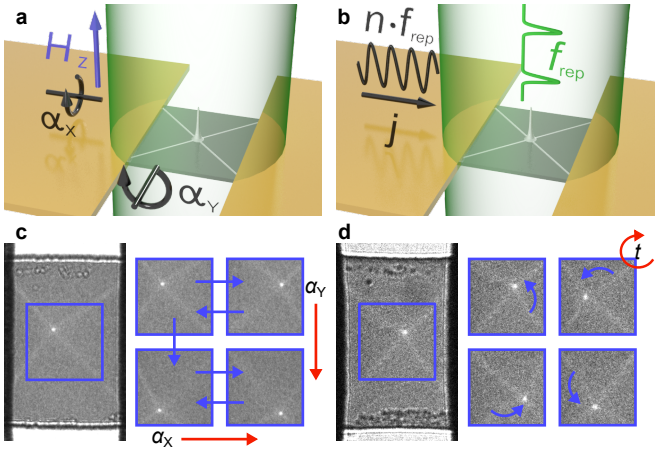

FIG. 1. (a) Sketch of the TRaPS measurement: The magnetic nanoisland (dark grey) is illuminated with a continuous collimated electron beam (green) and subjected to an external magnetic field H_z. Tilting the sample along the two tilt axes α_x and α_y enables us to move the vortex core within the nanostructure. (b) Sketch of the time-resolved experimental setup: Here, the nanoisland is imaged using a pulsed electron beam at a repetition rate of f_{rep} and excited with a synchronized alternating current at an integer multiple of the frequency of $f_{\mathrm{ex}} = n \cdot f_{\mathrm{rep}}$. (c) Four micrographs illustrating a TRaPS measurement. The vortex core is scanned horizontally back and forth across the island using α_x, while α_y is gradually increased to vertically offset the core in between scans, as is illustrated by the blue arrows. (d) Example of four time-resolved Lorentz-micrographs acquired at different time delays between exciting current and the pulsed electron beam. The bright lines indicate the position of the domain walls within the nanostructure, with their intersection marking the location of the vortex core. Between frames, the core is visibly displaced and moving on a counter-clockwise trajectory.

visually highlights the position of the four domain walls as bright lines (cf. Fig. 1 c). At their intersection, a peak is formed, marking the position of the vortex core. To perform a TRaPS measurement, we shift the core across the film in a rasterized fashion using in-plane magnetic fields and record Lorentz micrographs at each raster step. A repeated occurrence of the core at the same position can then indicate the location of a pinning site.

We generate the in-plane magnetic field components H_x, H_y along the x and y directions of the sample by applying an out-of-plane field H_z and tilting the sample along the two tilt axes α_x,α_y, as indicated in Figs. 1 a,c. For sufficiently small angles, the resulting field components are $(H_x, H_y) \approx H_z \cdot (\alpha_y, \alpha_x)$. The out-of-plane magnetic field H_z is generated by weakly exciting the main objective lens of the microscope while using the objective mini-lens for imaging.

C. Time-resolved Lorentz microscopy

Time-resolved Lorentz microscopy is carried out at the Göttingen ultrafast transmission electron microscope (UTEM), a modified JEOL 2100F transmission electron microscope (TEM) featuring a high-brightness photoemission electron source [37, 46]. For the present study, we equipped the UTEM with a radio-frequency (RF)-generator that is electronically synchronized to the photoemission laser, using a methodology introduced in Ref. [37]. One output of the RF-generator (Keysight 81160A) feeds into a custom TEM holder that enables TEM imaging under *in-situ* current excitation with frequencies up to the GHz regime. A second output triggers the photoemission laser, a gain-switched diode laser (custom Onefive Katana 05-HP) operating at a wavelength of 532 nm. With its continuously variable repetition rate of $f_{\mathrm{rep}} = 20 - 80\,\mathrm{MHz}$ and a pulse duration of 35 ps, this laser enables us to increase the electron-pulse duty cycle by more than two orders of magnitude compared to previous studies [37]. Thus, we can reduce the image acquisition time of a single stroboscopic micrograph from several minutes to a few seconds and compile much larger data sets that allow deeper insights into the vortex gyration.

We compile time-resolved movies of the vortex dynamics by exciting it at frequencies that are integer multiples of the laser repetition rate $f_{\mathrm{ex}} = n \cdot f_{\mathrm{rep}}$ and by incrementally changing the excitation phase between frames (see Fig. 1 b,d).

D. Bright-field imaging and vortex core localization

To assess the nanocrystalline structure of our samples, we recorded bright-field images in low-magnification mode (Figs. 2 a,b) by filtering out scattered parts of the beam using an aperture. This allows us to compare the vortex core positions we find in time-resolved and TRaPS measurements to the grain structure of the films. Therefore, we track the core in the Lorentz micrographs and map the results on top of the bright-field images. The tracking process involves calculating the center-of-mass of the pixels corresponding to the bright peak at the core position, which we identify as the largest pixel cluster above an intensity threshold. This method enables a core localization with few-nanometer precision [37]. To map the core positions onto the bright-field images, we use a geometric transformation [47], which is derived from the location of easily identifiable image features in both Lorentz and bright-field images. Using this approach, we can translate position information between both reference frames.

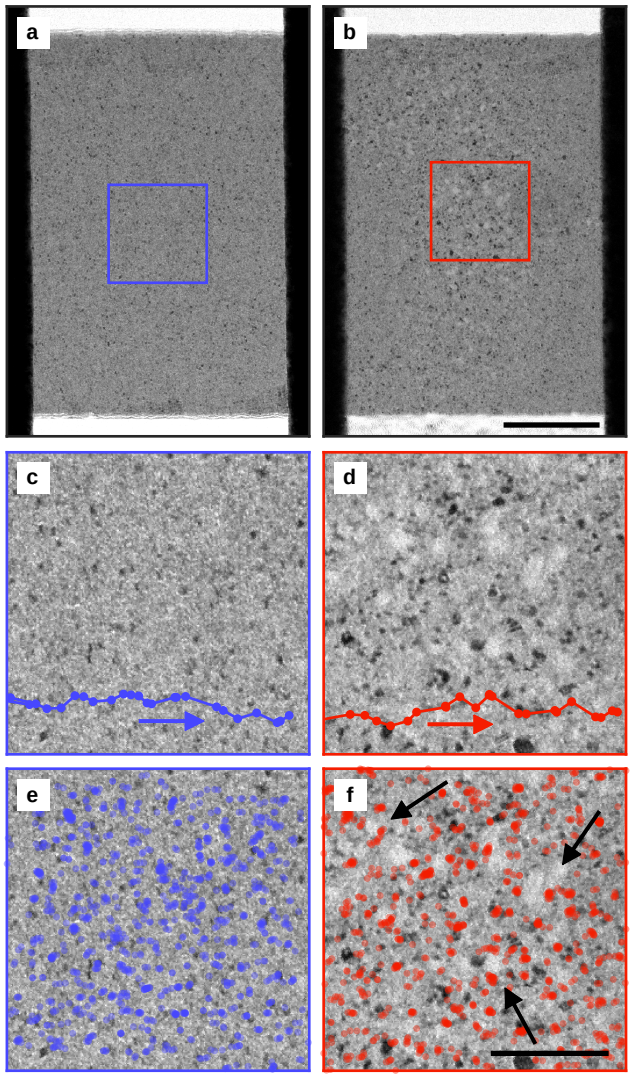

FIG. 2. Bright field images of the non-annealed sample **N1** (a) and the annealed sample **A** (b, 500 nm scalebar). (c,d) Close-ups of the regions marked in (a) and (b). The annealed sample shows a drastically increased grain size in the depicted area. The lines indicate the path of the vortex core during an exemplary tilt of primary tilt axis α_x, while α_y is kept constant. (d,e) Tracked vortex core positions overlaid on top of the bright-field images in (c) and (d) (200 nm scalebar).

III. RESULTS

A. TRaPS Measurements

TRaPS measurements are performed on the non-annealed sample **N1** and on sample **A**. In their bright-field images (Figs. 2 a,b), the bright and dark regions surrounding the grey permalloy nanostructure are bare silicon-nitride and the opaque gold contacts, respectively. A thin residue of permalloy, stemming from a partially coated undercut of the electron beam resist, is faintly vis-

ible at the top and bottom of the squares and can also be seen in the Lorentz images (e.g. Fig. 1 d). Contrast variations in the films arise from spatially varying diffraction conditions of differently oriented grains and reveal a significant increase in grain size in the annealed sample (cf. Figs. 2 c,d). This change in grain size is less significant in the vicinity of the gold contacts as these locally increase the thermal coupling, resulting in an inhomogeneous temperature profile during the annealing process.

For the TRaPS measurements, we apply an external field of $H_z = 35.8\,\mathrm{kA\,m^{-1}}$ and vary both tilt axes in a range from $-2.2°$ to $2.2°$ in increments of $0.2°$. Along the primary tilt direction α_x the samples are tilted back and forth once for every tilt position of the secondary axis α_y. Additionally, each sweep of α_x includes an approach step at either $\alpha_x = 3.0°$ or $-3.0°$. Supplementary Movies 1 and 2 show the complete TRaPS measurements of either sample, with some example micrographs of sample **N1** presented in Fig. 1 c.

As an example, we marked the path of the core during one sweep of α_x in Figs. 2 c,d, where we see that the core does not move in straight lines but rather zigzags and occasionally gets trapped. All tracked positions are marked with dots in Figs. 2 e,f where they are plotted on top of the bright-field image of the corresponding region. Due to the small size of the grains in sample **N1**, there is no apparent visual correspondence between the nanocrystalline structure and the core positions (Fig. 2 e). However, for the annealed sample **A**, we find numerous pinning sites located directly at boundaries of larger grains (see arrows Fig. 2 f). Furthermore, it stands out that the core never resides within one of the large grains. Both observations clearly demonstrate that grain boundaries can pin vortex cores in polycrystalline films. While this behavior was suspected before [29], it has, to our knowledge, never been directly observed.

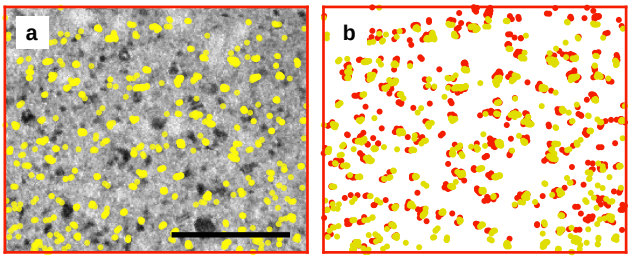

FIG. 3. Comparison between TRaPS measurement on sample **A** with clockwise curl $c = -1$ and underfocus imaging conditions (red dots) and counter-clockwise curl $c = +1$ and overfocus imaging conditions (yellow dots). (a) Tracked vortex core position overlaid onto bright-field image of sample **A** (200 nm scalebar). (b) Depiction of the tracked vortex position of both measurements in the reference frame of the bright-field image in (a). Both datasets are in good agreement with each other, with only a minor offset between the two. The difference in the overall center of both TRaPS measurements can be explained with a residual magnetic in-plane field at the sample position (see text).

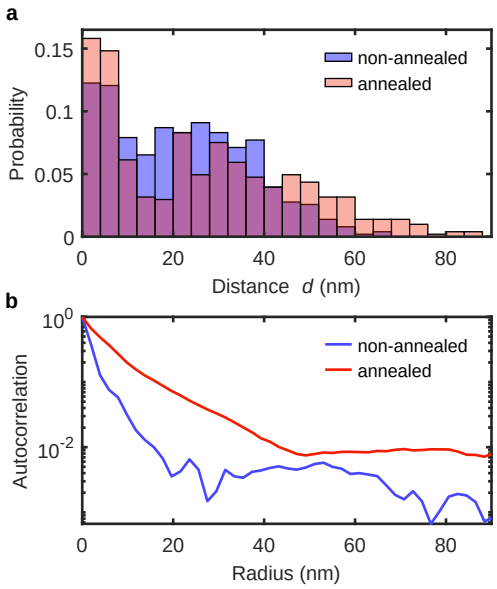

FIG. 4. (a) Probability that the vortex core moved by distance d between two TRaPS steps. (b) Radial autocorrelation of the bright field images displayed in Fig. 3 c,d.

To assess the accuracy of our measurement technique, we repeat the tracking and the transform calculation for a second set of experimental conditions on sample **A**. The results presented in Fig. 2 d are acquired with a clockwise curl ($c = -1$), necessitating underfocused imaging conditions to achieve a bright spot at the core position [48]. For the second measurement, we altered the domain state to a counter-clockwise curl ($c = +1$), and acquire overfocused Lorentz images (see Suppl. Movie 3). This second set of tracking data was likewise correlated with the bright-field image as shown in Fig. 3 a, and is in excellent agreement with the previous results. This is particularly evident when we plot both data sets together in the same reference frame as in Fig. 3 b, where the only discernible difference is a minor lateral displacement of about 6 nm. In addition to confirming that TRaPS allows for accurate localization of pinning sites, this comparison also demonstrates that the underlying process is independent of the vortex curl.

To further analyze our data, we calculate the distance d traveled by the vortex between two consecutive steps of a TRaPS scan. Fig. 4 b shows histograms of the jump distances for both samples (the initialization steps at $\alpha_x = \pm 3°$ are not included in these statistics). The most prominent feature in both distributions is a strong peak at small distances $d < 8\,\mathrm{nm}$. For these distances, we can assume that the vortex has remained at the same pinning site, and as we would expect, this happens more frequently for sample **A**. In contrast, we identify substantial differences between both samples for distances $d > 8\,\mathrm{nm}$: Firstly, the vortex in the annealed sample rarely moves by distances in the range of 8 nm to 20 nm, and secondly, it more frequently jumps over longer dis-

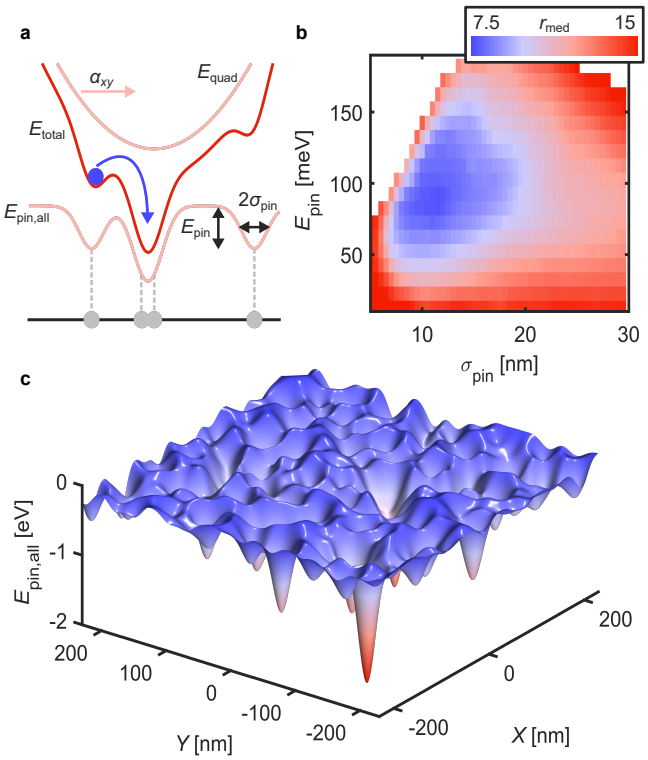

FIG. 5. Reconstruction of the pinning potential from TRaPS data of sample **N1**. (a) Illustration of model potential E_{total} used for the simulated TRaPS data. E_{quad} is a quadratic plus a field-dependent linear potential (here, as a function of the tilt angle $\alpha_{x,y}$) that defines the equilibrium position of the vortex core in the absence of any pinning. $E_{\text{pin,all}}$ is composed of a Gaussian potentials for each experimentally measured pinning position (grey dots), all having the same depth E_{pin} and width σ_{pin}. By increasing/decreasing the tilt angle, the vortex core is dragged along and probes the pinning potential. (b) Median radial deviation r_{med} between the experimental and simulated TRaPS data for various combinations of E_{pin} and width σ_{pin}. The best agreement is obtained at $r_{\text{med}} = 7.6\,\text{nm}$ with $E_{\text{pin}} = 80\,\text{meV}$ and $\sigma_{\text{pin}} = 11\,\text{nm}$. Values of E_{pin} and σ_{pin} which do not improve r_{med}, compared to a case of no pinning potential, are left blank. (c) 2D representation of the pinning potential $E_{\text{pin,all}}$ for $E_{\text{pin}} = 80\,\text{meV}$ and $\sigma_{\text{pin}} = 11\,\text{nm}$.

tances beyond 40 nm, which evidently is a result of larger grain sizes.

For comparison, we also compute the average grain size in both samples using the full-width-half-maximum of the radial autocorrelation function [49, 50][51]. From the autocorrelation functions in Fig. 4 we estimate grain sizes of 4 nm and 10 nm for sample **N1** and **A**, respectively. This demonstrates that the typical jump distances span up to several grain diameters, suggesting that not every grain boundary causes effective pinning.

B. Quantifying the Pinning Potential

In order to extract the pinning energy landscape from our TRaPS measurement, we compare experimental with simulated TRaPS data. Therefore, we model the movement of the vortex core in a global quadratic plus a local pinning potential, as illustrated in Fig. 5 a. By scanning the quadratic potential across the disorder potential, we replicate how the core is trapped and moves between pinning sites.

We define the quadratic potential using the rigid vortex model [52], for which the energy of the vortex domain configuration is expressed in terms of the core position (X, Y) and the external magnetic field

$$E_{\text{quad}} = \frac{1}{2}k(X^2 + Y^2) + ck\chi\left(-H_x Y + H_y X\right) . \quad (1)$$

Here, k is the stiffness factor of the quadratic potential, and χ is the displacement susceptibility. For our sample geometry, we calculate a stiffness factor of $k = 1.63 \times 10^{-3}\,\text{eV nm}^{-2}$ using micromagnetic simulations [53]. The simulation is performed with a $512 \times 512 \times 4$ cell geometry, an exchange coupling of $A_{\text{ex}} = 1.11 \times 10^{-11}\,\text{J m}^{-1}$ [54], and a saturation magnetization of $M_{\text{S}} = 440\,\text{kA m}^{-1}$[55].

The equilibrium core position, i.e., the minimum of E_{quad}, is given by

$$\begin{pmatrix} X \\ Y \end{pmatrix} = c\chi \begin{pmatrix} -H_y \\ H_x \end{pmatrix} = c\underbrace{\chi H_z}_{=:\tilde{\chi}} \begin{pmatrix} -\alpha_x \\ \alpha_y \end{pmatrix} . \quad (2)$$

Here, we replace χ with a modified displacement susceptibility $\tilde{\chi} = \chi H_z$, which specifies the core movement per tilt angle. By fitting Eq. 2 to our data, we find $\tilde{\chi}$ to be 98 nm/° and 108 nm/° for sample **N1** and **A**, respectively. This is in good agreement with the micromagnetic simulation, which predicted a value of $\tilde{\chi} = 123\,\text{nm}/°$.

To simulate the behavior of the pinning sites, we place a Gaussian-potential dip with depth E_{pin} and width σ_{pin} at every position $(X_{i,\text{exp}}, Y_{i,\text{exp}})$ tracked in the TRaPS measurement (see Fig. 5a). This ensures a deeper and/or broader potential in regions where the core is encountered more frequently. The pinning potential is hence given by

$$E_{\text{pin,all}} = -E_{\text{pin}} \sum_i \exp\left(-\frac{r_i^2}{2\sigma_{\text{pin}}^2}\right) , \quad (3)$$

where $r_i^2 = (X - X_{i,\text{exp}})^2 + (Y - Y_{i,\text{exp}})^2$ is the distance to the core position measured at tilt step i of the TRaPS measurement. The total potential is thus $E_{\text{total}} = E_{\text{quad}} + E_{\text{pin,all}}$.

In the course of a single simulation we set the same sequence of tilt angles and, at each tilt step i, find the next local minimum $(X_{i,\text{sim}}, Y_{i,\text{sim}})$ of E_{total} in the direction of steepest descent. The starting point of this minimization is the simulated minimum from the previous tilt step $i-1$, just like in the experiment. This leaves us with a set

of simulated core positions from which we can calculate the median radial deviation

$$r_{\mathrm{med}} = \mathrm{median}_i \left(\left\| \begin{matrix} X_{i,\mathrm{sim}} - X_{i,\mathrm{exp}} \\ Y_{i,\mathrm{sim}} - Y_{i,\mathrm{exp}} \end{matrix} \right\| \right) . \qquad (4)$$

Lastly, we find the combination of E_{pin} and σ_{pin} (the only free parameters in our model) that minimizes r_{med} and thus best represents our experimental data.

Figure 5 b shows the median radial deviation for all simulations based on the TRaPS measurement of sample **N1**. It is minimum at $E_{\mathrm{pin}} = 80\,\mathrm{meV}$ and $\sigma_{\mathrm{pin}} = 11\,\mathrm{nm}$. In case of sample **A**, we obtain similar values of $E_{\mathrm{pin}} = 90\,\mathrm{meV}$ and $\sigma_{\mathrm{pin}} = 12\,\mathrm{nm}$, which results in an increase of the integrated pinning potential of about 30 %. The simulated core positions are in good agreement with experimental data, as we present in Suppl. Fig. 7, together with images of the pinning potential.

A three-dimensional representation of $E_{\mathrm{pin,all}}$ of sample **N1** is given in Fig. 5 c. It has a roughness, estimated by the standard deviation of the potential, of 193 meV and measures −2.0 eV at its deepest point. For the annealed sample, the respective values are 281 meV and −2.4 eV. This analysis demonstrates that polycrystalline samples with larger grains show an overall increase in their pinning potential, with an increased roughness and deeper minima. Furthermore, we note that the demonstrated method is capable of quantifying pinning potentials down to sub-100 meV and spanning multiple orders of magnitude.

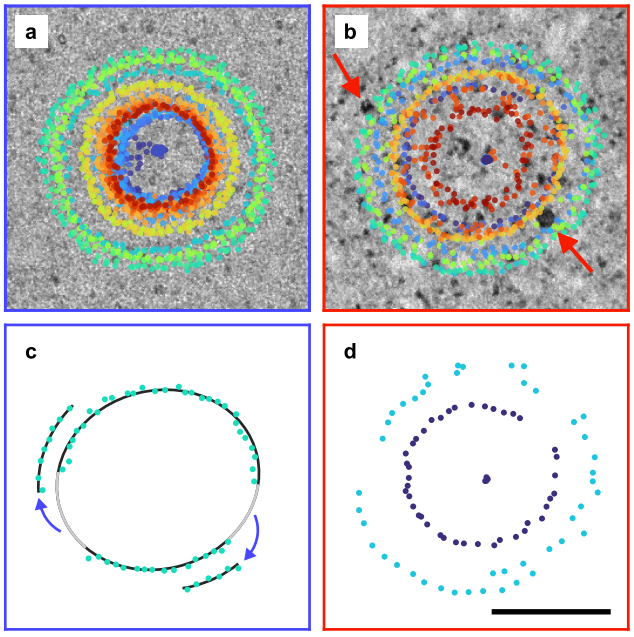

FIG. 6. (a,b) Trajectories (dots) of the vortex gyration in sample **N2** (a) and sample **A** (b) measured via time-resolved Lorentz microscopy overlaid on top of bright-field images of samples. Each color corresponds to a specific frequency according to the colorbar given in Fig. 7. (c) Example of a segmented trajectory in (a) indicating a bistable gyration. The black line is a guide to the eye, indicating the movement of the core. The greyed-out path and the arrows indicate where the core jumped to another equally favorable orbit. (d) Two examples for jagged trajectories in (b) (200 nm scalebar).

C. Time-resolved Trajectories

Besides studying the static interaction of the vortex core with pinning sites, we also probed how the dynamic vortex gyration is affected by the nanocrystalline configuration. We therefore perform time-resolved measurements on the non-annealed sample **N2** and the annealed sample **A**, where we excite the permalloy square with an alternating current forcing the vortex core on an elliptical trajectory. We recorded this motion in sample **N2** for excitation frequencies from $f_{\mathrm{ex}} = 86\,\mathrm{MHz}$ to 99.5 MHz at a current density of $j = 3.6 \times 10^{10}\,\mathrm{A_{rms}\,m^{-2}}$ and in case of sample **A** for frequencies from 72 MHz to 84 MHz at $j = 8.2 \times 10^{10}\,\mathrm{A_{rms}\,m^{-2}}$. The higher currents and lower frequencies in the case of sample **A** were only necessary after annealing, whereas before, we were able to observe core gyration at similar excitation parameters as for sample **N2**. To measure and ensure a constant excitation current throughout the frequency range, we monitor the sample current I_{S} using an oscilloscope (for details, see Suppl. Note 1).

At each frequency, we record up to 60 micrographs and incrementally increase the phase between the RF-current and the probing electron beam to cover the whole excitation period. These micrographs are combined into Supp. Movies 4 and 5, and show the time-resolved gyration together with the tracked core positions. Figures 6 a,b show a compilation of all trajectories overlaid on the bright-field images (individual depictions in Suppl. Figs. 5 and 6).

Similar to our TRaPS measurements, we can also identify grains in the annealed sample in Fig. 6 b that appear to be avoided by the core, however, less conclusively as in the static case. We marked two of these grains with arrows in Fig. 6 b. Furthermore, we find discontinuous jumps of the vortex position upon cycling the excitation phase, where it appears to switch between two or more equally favorable trajectories. Interestingly, this behavior is encountered much more regularly for the annealed sample, both at a larger number of frequencies and during a measurement at a given frequency (see Supp. Figs. 5 and 6). Most likely, the jumps between multistable orbits are triggered by the sudden (yet small) change of the excitation phase between time-resolved micrographs. This multistability can be considered the dynamic counterpart of stochastic switching between bistable static pinning sites [24, 30, 56].

To further evaluate the trajectories, we fit them to an ellipse and determine the mean of both semiaxes r [57]. Figure 7 shows the resulting radii r diveded by the sample current I_{S} and plotted against the normalized frequency $f_{\mathrm{ex}}/f_{\mathrm{r}}$. The graphs reveal a resonance frequency of the

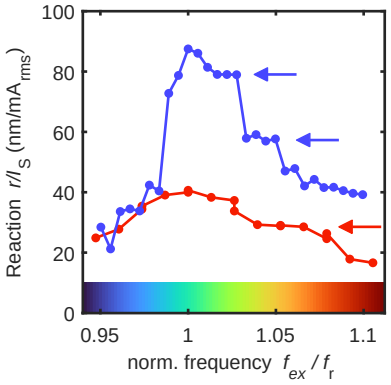

FIG. 7. Excitation-current-normalized radius r/I_S as a function of normalized frequency f_{ex}/f_r. For some frequency ranges the orbit radius stays constant upon changing the excitation frequency (arrows).

gyration of $f_r = 90.5\,\mathrm{MHz}$ and 76 MHz for sample **N2** and **A**, respectively. Here, two observations stand out. First, the radius of the trajectories does not change continuously in size as a function of frequency f_{ex} (see also Refs. [37, 42]), suggesting hysteretic behavior. Instead, we find plateaus, for which trajectories cluster at certain radii (marked with arrows in Fig. 7), clearly indicating an orbital stabilization by the pinning potential. Secondly, we find that the current-normalized radius r/I_S is significantly smaller and exhibits a broader resonance in the case of the annealed sample **A**, which is a distinct sign of enhanced dissipation in this sample. These two observations, together with enhanced multistability in the annealed sample, demonstrate that grain sizes have an important influence on the dynamic behavior of gyrating vortices.

IV. CONCLUSION

Nanocrystallinity and surface roughness have long been linked to the pinning of vortices in soft-magnetic films [21, 27, 29]. The direct real-space identification of grain boundaries as effective pinning sites for the core was enabled by the TRaPS method introduced in this study. The correlation of structural and magnetic imaging in electron microscopy can be further developed to trace the microscopic origins of pinning down to the atomic scale, combining high-resolution (scanning) TEM with holography [58, 59] or differential phase contrast [33, 60].

The joint high spatial and temporal resolution of our approach will be critical to explore transient pinning and local damping effects, while the quantitative TRaPS potential will serve as input for future theoretical studies on driven vortex dynamics. The global ansatz for the calculation of the trapping potential based on common properties of pinning sites may be further refined by taking into consideration characteristics of individual defects. The observation of increased roughness, deeper traps and enhanced bistability for samples with larger grains may become relevant for device fabrication and in the tailoring of annealing processes to mitigate or selectively enhance pinning.

Finally, on the methodical side, the two orders of magnitude increase in time-averaged brightness of the photoemission source will have immediate benefits in picosecond stroboscopic imaging of ultrafast dynamics also beyond magnetism, including nanoscale structural and electronic phenomena.

ACKNOWLEDGMENTS

This work was funded by the Deutsche Forschungsgemeinschaft (DFG) in the Collaborative Research Center "Atomic Scale Control of Energy Conversion" (DFG-SFB 1073, project A05) and via resources from the Gottfried Wilhelm Leibniz-Prize. We gratefully acknowledge support by the Lower Saxony Ministry of Science and Culture and funding of the instrumentation by the DFG and VolkswagenStiftung. Furthermore, we acknowledge helpful discussions and assistance from the Göttingen UTEM Team, especially Thomas Danz, Till Domröse, Armin Feist and Karin Ahlborn.

C.R. and M.M. conceived the project. M.M. prepared the sample. M.M. and J.H.G. conducted the experiment. M.M. evaluated the data and discussed the results with J.H.G. and C.R. M.M. and C.R. wrote the paper with inputs from J.H.G.

[1] A. Hubert and R. Schäfer, *Magnetic domains: the analysis of magnetic ...* (Springer, Berlin, Heidelberg, 1998).
[2] T. Shinjo, T. Okuno, R. Hassdorf, K. Shigeto, and T. Ono, Magnetic Vortex Core Observation in Circular Dots of Permalloy, Science **289**, 930 (2000).
[3] T. Eggebrecht, M. Möller, J. G. Gatzmann, N. Rubiano da Silva, A. Feist, U. Martens, H. Ulrichs, M. Münzenberg, C. Ropers, and S. Schäfer, Light-Induced Metastable Magnetic Texture Uncovered by in situ Lorentz Microscopy, Physical Review Letters **118**, 097203 (2017), arXiv:1609.04000.
[4] T. Skyrme, A unified field theory of mesons and baryons, Nuclear Physics **31**, 556 (1962).
[5] S. Mühlbauer, B. Binz, F. Jonietz, C. Pfleiderer, A. Rosch, A. Neubauer, R. Georgii, and P. Boni, Skyrmion Lattice in a Chiral Magnet, Science **323**, 915 (2009).
[6] X. Z. Yu, Y. Onose, N. Kanazawa, J. H. Park, J. H. Han, Y. Matsui, N. Nagaosa, and Y. Tokura, Real-space observation of a two-dimensional skyrmion crystal, Nature

465, 901 (2010), arXiv:arXiv:1103.0321.

[7] S. S. P. Parkin, M. Hayashi, and L. Thomas, Magnetic Domain-Wall Racetrack Memory, Science **320**, 190 (2008), arXiv:arXiv:1011.1669v3.

[8] N. S. Kiselev, A. N. Bogdanov, R. Schäfer, and U. K. Rößler, Chiral skyrmions in thin magnetic films: new objects for magnetic storage technologies?, Journal of Physics D: Applied Physics **44**, 392001 (2011), arXiv:1102.2726.

[9] A. Fert, V. Cros, and J. Sampaio, Skyrmions on the track, Nature Nanotechnology **8**, 152 (2013), arXiv:1008.2287v1.

[10] A. Fert, N. Reyren, and V. Cros, Magnetic skyrmions: advances in physics and potential applications, Nature Reviews Materials **2**, 17031 (2017).

[11] H. Jung, Y.-S. Choi, K.-S. Lee, D.-S. Han, Y.-S. Yu, M.-Y. Im, P. Fischer, and S.-K. Kim, Logic Operations Based on Magnetic-Vortex-State Networks, ACS Nano **6**, 3712 (2012).

[12] X. Zhang, M. Ezawa, and Y. Zhou, Magnetic skyrmion logic gates: conversion, duplication and merging of skyrmions, Scientific Reports **5**, 9400 (2015), arXiv:1410.3086.

[13] J. Torrejon, M. Riou, F. A. Araujo, S. Tsunegi, G. Khalsa, D. Querlioz, P. Bortolotti, V. Cros, K. Yakushiji, A. Fukushima, H. Kubota, S. Yuasa, M. D. Stiles, and J. Grollier, Neuromorphic computing with nanoscale spintronic oscillators, Nature **547**, 428 (2017).

[14] S.-B. Choe, Vortex Core-Driven Magnetization Dynamics, Science **304**, 420 (2004), arXiv:1002.1037.

[15] B. Van Waeyenberge, A. Puzic, H. Stoll, K. W. Chou, T. Tyliszczak, R. Hertel, M. Fähnle, H. Brückl, K. Rott, G. Reiss, I. Neudecker, D. Weiss, C. H. Back, and G. Schütz, Magnetic vortex core reversal by excitation with short bursts of an alternating field, Nature **444**, 461 (2006).

[16] K. Yamada, S. Kasai, Y. Nakatani, K. Kobayashi, H. Kohno, A. Thiaville, and T. Ono, Electrical switching of the vortex core in a magnetic disk, Nature Materials **6**, 270 (2007), arXiv:0702589 [cond-mat].

[17] S. Woo, K. Litzius, B. Krüger, M.-Y. Im, L. Caretta, K. Richter, M. Mann, A. Krone, R. M. Reeve, M. Weigand, P. Agrawal, I. Lemesh, M.-A. Mawass, P. Fischer, M. Kläui, and G. S. D. Beach, Observation of room-temperature magnetic skyrmions and their current-driven dynamics in ultrathin metallic ferromagnets, Nature Materials **15**, 501 (2016).

[18] K. Gerlinger, B. Pfau, F. Büttner, M. Schneider, L.-M. Kern, J. Fuchs, D. Engel, C. M. Günther, M. Huang, I. Lemesh, L. Caretta, A. Churikova, P. Hessing, C. Klose, C. Strüber, C. V. K. Schmising, S. Huang, A. Wittmann, K. Litzius, D. Metternich, R. Battistelli, K. Bagschik, A. Sadovnikov, G. S. D. Beach, and S. Eisebitt, Application concepts for ultrafast laser-induced skyrmion creation and annihilation, Applied Physics Letters **118**, 192403 (2021).

[19] S. G. Je, P. Vallobra, T. Srivastava, J. C. Rojas-Sánchez, T. H. Pham, M. Hehn, G. Malinowski, C. Baraduc, S. Auffret, G. Gaudin, S. Mangin, H. Béa, and O. Boulle, Creation of Magnetic Skyrmion Bubble Lattices by Ultrafast Laser in Ultrathin Films, Nano Letters **18**, 7362 (2018), arXiv:1808.01385.

[20] M. Rahm, R. Höllinger, V. Umansky, and D. Weiss, Influence of point defects on magnetic vortex structures, Journal of Applied Physics **95**, 6708 (2004).

[21] T. Uhlig, M. Rahm, C. Dietrich, R. Höllinger, M. Heumann, D. Weiss, and J. Zweck, Shifting and Pinning of a Magnetic Vortex Core in a Permalloy Dot by a Magnetic Field, Physical Review Letters **95**, 237205 (2005).

[22] A. Vansteenkiste, J. De Baerdemaeker, K. W. Chou, H. Stoll, M. Curcic, T. Tyliszczak, G. Woltersdorf, C. H. Back, G. Schütz, and B. Van Waeyenberge, Influence of domain wall pinning on the dynamic behavior of magnetic vortex structures: Time-resolved scanning x-ray transmission microscopy in NiFe thin film structures, Physical Review B **77**, 144420 (2008).

[23] C. Holl, M. Knol, M. Pratzer, J. Chico, I. L. Fernandes, S. Lounis, and M. Morgenstern, Probing the pinning strength of magnetic vortex cores with sub-nanometer resolution, Nature Communications **11**, 2833 (2020), arXiv:2001.06682.

[24] J. A. J. Burgess, A. E. Fraser, F. F. Sani, D. Vick, B. D. Hauer, J. P. Davis, and M. R. Freeman, Quantitative Magneto-Mechanical Detection and Control of the Barkhausen Effect, Science **339**, 1051 (2013).

[25] R. L. Compton and P. A. Crowell, Dynamics of a Pinned Magnetic Vortex, Physical Review Letters **97**, 137202 (2006), arXiv:0607095 [cond-mat].

[26] R. L. Compton, T. Y. Chen, and P. A. Crowell, Magnetic vortex dynamics in the presence of pinning, Physical Review B **81**, 144412 (2010).

[27] T. Y. Chen, M. J. Erickson, P. A. Crowell, and C. Leighton, Surface Roughness Dominated Pinning Mechanism of Magnetic Vortices in Soft Ferromagnetic Films, Physical Review Letters **109**, 097202 (2012), arXiv:arXiv:1201.1334v1.

[28] T. Y. Chen, A. T. Galkiewicz, and P. A. Crowell, Phase diagram of magnetic vortex dynamics, Physical Review B **85**, 180406 (2012).

[29] R. Badea and J. Berezovsky, Mapping the Landscape of Domain-Wall Pinning in Ferromagnetic Films Using Differential Magneto-Optical Microscopy, Physical Review Applied **5**, 064003 (2016).

[30] R. Badea, M. S. Wolf, and J. Berezovsky, Exploiting bistable pinning of a ferromagnetic vortex for nitrogen-vacancy spin control, Applied Physics Letters **109**, 10.1063/1.4963670 (2016).

[31] J.-S. Kim, O. Boulle, S. Verstoep, L. Heyne, J. Rhensius, M. Kläui, L. J. Heyderman, F. Kronast, R. Mattheis, C. Ulysse, and G. Faini, Current-induced vortex dynamics and pinning potentials probed by homodyne detection, Physical Review B **82**, 104427 (2010).

[32] C. Hanneken, A. Kubetzka, K. von Bergmann, and R. Wiesendanger, Pinning and movement of individual nanoscale magnetic skyrmions via defects, New Journal of Physics **18**, 055009 (2016), arXiv:1601.05204.

[33] S. McVitie, D. McGrouther, S. McFadzean, D. MacLaren, K. O'Shea, and M. Benitez, Aberration corrected Lorentz scanning transmission electron microscopy, Ultramicroscopy **152**, 57 (2015).

[34] K. B. Schliep, P. Quarterman, J.-P. P. Wang, and D. J. Flannigan, Picosecond Fresnel transmission electron microscopy, Applied Physics Letters **110**, 222404 (2017).

[35] N. Rubiano da Silva, M. Möller, A. Feist, H. Ulrichs, C. Ropers, and S. Schäfer, Nanoscale Mapping of Ultrafast Magnetization Dynamics with Femtosecond Lorentz Microscopy, Physical Review X **8**, 031052 (2018),

arXiv:1710.03307.
[36] M. Zhang, Z.-A. Li, S. Sun, P. Xu, C. Zhu, H. Tian, Z. Li, Y. Zhang, H. Yang, and J. Li, High Spatiotemporal Resolution ofMagnetic Dynamics in Mn-Ni-Ga via Four-Dimensional Lorentz Microscopy Ming, Physical Review Applied **12**, 034037 (2019).
[37] M. Möller, J. H. Gaida, S. Schäfer, and C. Ropers, Few-nm tracking of current-driven magnetic vortex orbits using ultrafast Lorentz microscopy, Communications Physics **3**, 36 (2020).
[38] X. Fu, E. Wang, Y. Zhao, A. Liu, E. Montgomery, V. J. Gokhale, J. J. Gorman, C. Jing, J. W. Lau, and Y. Zhu, Direct visualization of electromagnetic wave dynamics by laser-free ultrafast electron microscopy, Science Advances **6**, eabc3456 (2020).
[39] G. Cao, S. Jiang, J. Åkerman, and J. Weissenrieder, Femtosecond laser driven precessing magnetic gratings, Nanoscale **13**, 3746 (2021).
[40] S. Kasai, Y. Nakatani, K. Kobayashi, H. Kohno, and T. Ono, Current-Driven Resonant Excitation of Magnetic Vortices, Physical Review Letters **97**, 107204 (2006).
[41] M. Bolte, G. Meier, B. Krüger, A. Drews, R. Eiselt, L. Bocklage, S. Bohlens, T. Tyliszczak, A. Vansteenkiste, B. Van Waeyenberge, K. W. Chou, A. Puzic, and H. Stoll, Time-Resolved X-Ray Microscopy of Spin-Torque-Induced Magnetic Vortex Gyration, Physical Review Letters **100**, 176601 (2008), arXiv:0801.4719.
[42] S. Pollard, L. Huang, K. Buchanan, D. Arena, and Y. Zhu, Direct dynamic imaging of non-adiabatic spin torque effects, Nature Communications **3**, 1028 (2012).
[43] B. Krüger, A. Drews, M. Bolte, U. Merkt, D. Pfannkuche, and G. Meier, Harmonic oscillator model for current- and field-driven magnetic vortices, Physical Review B **76**, 224426 (2007), arXiv:0710.0532.
[44] M. De Graef, *Experimental Methods in the Physical Sciences*, Experimental Methods in the Physical Sciences, Vol. 36 (CRC Press, 2001) pp. 27–67.
[45] J. Zweck, Imaging of magnetic and electric fields by electron microscopy, Journal of Physics: Condensed Matter **28**, 403001 (2016).
[46] A. Feist, N. Bach, N. Rubiano da Silva, T. Danz, M. Möller, K. E. Priebe, T. Domröse, J. G. Gatzmann, S. Rost, J. Schauss, S. Strauch, R. Bormann, M. Sivis, S. Schäfer, and C. Ropers, Ultrafast transmission electron microscopy using a laser-driven field emitter: Femtosecond resolution with a high coherence electron beam, Ultramicroscopy **176**, 63 (2017), arXiv:1611.05022.
[47] A. Goshtasby, Image registration by local approximation methods, Image and Vision Computing **6**, 255 (1988).
[48] M. Schneider, H. Hoffmann, and J. Zweck, Lorentz microscopy of circular ferromagnetic permalloy nanodisks, Applied Physics Letters **77**, 2909 (2000).
[49] R. P. Heilbronner, The autocorrelation function: an image processing tool for fabric analysis, Tectonophysics **212**, 351 (1992).
[50] B. Zang, K. Suzuki, and A. C. Liu, Estimation of volume-weighted average grain size in Fe-based nanocrystalline soft magnetic materials by autocorrelation function, Materials Characterization **142**, 577 (2018).
[51] It is worth noting that dark-field images were used for this assessment in the original publications. However, we believe that for a rough estimate, we are interested here, bright-field images are equally suitable.
[52] K. Y. Guslienko, V. Novosad, Y. Otani, H. Shima, and K. Fukamichi, Field evolution of magnetic vortex state in ferromagnetic disks, Applied Physics Letters **78**, 3848 (2001).
[53] A. Vansteenkiste, J. Leliaert, M. Dvornik, M. Helsen, F. Garcia-Sanchez, and B. Van Waeyenberge, The design and verification of MuMax3, AIP Advances **4**, 137133 (2014), arXiv:1406.7635.
[54] Y. Yin, F. Pan, M. Ahlberg, M. Ranjbar, P. Dürrenfeld, A. Houshang, M. Haidar, L. Bergqvist, Y. Zhai, R. K. Dumas, A. Delin, and J. Åkerman, Tunable permalloy-based films for magnonic devices, Physical Review B **92**, 024427 (2015).
[55] This value was obtained from a comparison of experimental and simulated Lorentz images, using the nominal film thickness of 30 nm. It is somewhat lower than expected from bulk values, which might be caused by uncertainty in the determination of the film thickness.
[56] R. Badea, E. Haber, and J. Berezovsky, Stochastic Dynamics of a Ferromagnetic Vortex Revealed by Single-Spin Magnetometry, Physical Review Applied **10**, 064031 (2018).
[57] O. Gal, fit_ellipse - File Exchange - MATLAB Central (2003).
[58] H. Lichte and M. Lehmann, Electron holography—basics and applications, Reports on Progress in Physics **71**, 016102 (2008).
[59] P. A. Midgley and R. E. Dunin-Borkowski, Electron tomography and holography in materials science, Nature Materials **8**, 271 (2009).
[60] J. N. Chapman, P. E. Batson, E. M. Waddell, and R. P. Ferrier, The direct determination of magnetic domain wall profiles by differential phase contrast electron microscopy, Ultramicroscopy **3**, 203 (1978).